X-Ray Orientation Microscopy using Topo-tomography and multi-mode Diffraction Contrast Tomography

Nicola Viganò, Wolfgang Ludwig

X-Ray Orientation Microscopy using Topo-tomography and multi-mode Diffraction Contrast Tomography

Nicola Viganò[a,b], Wolfgang Ludwig[c,a,*]

[a] *ESRF - The European Synchrotron, Grenoble, France*
[b] *Centrum Wiskunde & Informatica (CWI), NWO, Amsterdam, The Netherlands*
[c] *Univ Lyon, INSA Lyon, CNRS, MATEIS UMR5510, France*

Abstract

Polycrystal orientation mapping techniques based on full-field acquisition schemes like X-ray Diffraction Contrast Tomography and certain other variants of 3D X-Ray Diffraction or near-field High Energy Diffraction Microscopy enable time efficient mapping of 3D grain microstructures. The spatial resolution obtained with this class of monochromatic beam X-ray diffraction imaging approaches remains typically below the ultimate spatial resolution achievable with X-ray imaging detectors. Introducing a generalised reconstruction framework enabling the combination of acquisitions with different detector pixel size and sample tilt settings provide a pathway towards 3D orientation mapping with a spatial resolution approaching the one of state of the art X-ray imaging detector systems.

1. Introduction

Experimental capabilities to map crystal orientation and elastic strain fields in the bulk of polycrystalline materials by means of X-ray diffraction have seen tremendous progress over the past years. A whole portfolio of different X-ray diffraction based techniques have reached maturity and are now routinely applied to a broad variety of topics in materials science covering fields like grain coarsening [1, 2], plastic deformation [3, 4], various modes of materials failure [5, 6, 7] and phase transformations [8, 9].

Very much like modern electron microscopes offer a variety of imaging and diffraction modes in the same instrument, state of the art synchrotron beamlines

*Corresponding author
Email address: ludwig@esrf.fr (Wolfgang Ludwig)

offer multi-modal X-ray characterization. In the case of the materials science beamline at the European Synchrotron Radiation Facility this portfolio includes phase contrast tomography (PCT) [10, 11] as a Fresnel diffraction based imaging mode, diffraction contrast tomography (DCT) [12] as a Bragg diffraction based imaging mode for mapping the grain structure in polycrystalline sample volumes, and Topo-tomography (TT) [13] as a Bragg diffraction based imaging mode for mapping individual grains by rotation around one of the scattering vectors. These techniques typically employ high resolution imaging detectors (0.5-5 μm), whereas so-called far-field techniques like three-dimensional X-ray diffraction (3DXRD), as well as (nano) scanning X-ray diffraction computed tomography (nXRD-CT) [14] employ diffraction detectors with larger pixels (50-200 μm). These latter techniques typically yield sufficient angular resolution to reveal the small elastic distortions of the crystal unit cell and are therefore often used to obtain complementary information in strained materials [15, 16] (see also contribution by J. Wright for more details on these last two techniques and the Materials Science endstation ID11 at ESRF).

The data generated by imaging or diffraction modalities are usually reconstructed independently and results are combined in a post-processing step, as illustrated in previous studies of stress corrosion cracking [5] and fatigue cracking [6, 17, 18] which captured crack propagation by repeated PCT observations on grain microstructures which were previously characterized by 3D grain mapping techniques on the same instrument and during the same experimental session. There are, however, also first examples of combined analysis schemes for data acquired in different diffraction modalities. For instance, grain shape reconstructions by near-field High Energy Diffraction Microscopy (NF-HEDM) [19] are commonly seeded by indexing information obtained from far-field (FF-HEDM) [20] and instrument alignment for topo-tomographic observations of individual grains is inferred from concomitant DCT observations [21, 22].

The ultimate spatial resolution of near-field polycrystal grain mapping techniques is inherently limited by the need to capture diffraction signals from a number of different *hkl* reflections. For instance, for metals with highly symmetric crystal structures, the X-ray imaging detector is typically positioned at a distance such that the innermost 3 to 5 *hkl* families are intercepted by the

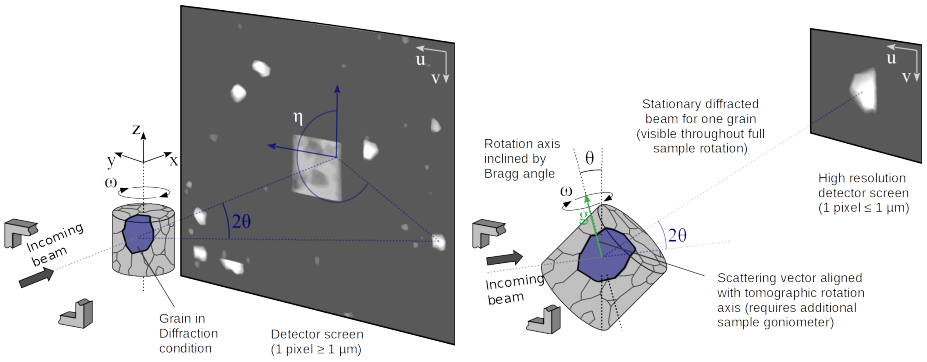

(a) DCT (b) TT

Figure 1: Schematic representation of two instances of X-Ray Diffraction experimental setups: (a) DCT enables 3D mapping of polycrystalline sample volumes. The sample rotation axis z is set perpendicular to the X-ray beam x; *(x,y,z)* represent the laboratory reference frame. (b) Topotomography for high resolution mapping of individual grains: the sample is tilted such that it can be rotated around one of the scattering vectors. The rotation axis is inclined by the Bragg angle (requires diffractometer.)

screen, giving rise to several tens up to hundred observable diffraction blobs per grain. In order to avoid overlaps between the transmitted and the diffracted beams, the footprint of the illuminated sample volume has to be kept small and it typically does not exceed one quarter of the lateral dimensions of the detector. Consequently, in the limiting case of a single crystal, the ultimate spatial resolution of the resulting grainmap is already compromised by a factor of four with respect to the full resolution of the detector system. For polycrystalline samples containing up to ten and more grains through-thickness the spatial sampling (number of voxels per grain) degrades accordingly and the physical voxel size in the resulting grain map is often well below the ultimate spatial resolution achievable with state of the art X-ray imaging detectors (see Fig. 1).

In order to overcome the limits in resolution dictated by the detector system, two options exist: one can either focus the beam and switch to a 3D point scanning approach like nXRD-CT [14, 23] or one can "zoom-in" on individual grains inside the sample volume using Dark Field X-ray Microscopy (DFXM) [24, 25]. Both methods can provide access to sub-micrometer spatial resolution which, neglecting instrument error motion and sample drifts, is ultimately limited by

the performance of the X-ray optical elements. However, in both cases this gain in spatial resolution comes at the expense of reduced temporal resolution, since these methods imply multi-dimensional scanning procedures (see contributions by H. Simons et al. and J. Wright et al. for more detail on these techniques).

In this article, we propose a different strategy to improve the spatial resolution of full-field grain mapping techniques. As will be shown, the combination of limited projection data acquired at high spatial resolution (e.g. TT scans of individual grains or partial near-field diffraction data acquired on a high resolution detector covering only the innermost *hkl* families) with data acquired in the conventional setting at lower spatial resolution can result in significant improvements in the overall reconstruction quality.

In order to enable joint reconstruction of the 3D orientation field from disparate projection data (i.e. different detector positions, rotation axis, pixel resolution and sample tilt settings) we introduce a generalization of the six-dimensional reconstruction framework proposed by Poulsen [26] and Viganò [27, 28]. This model builds on kinematical diffraction and we further assume that the position, average orientation and the orientation space sub-volume occupied by the grain are known from previous polycrystal indexing and analysis steps, not further detailed here. In a nutshell, in addition to the regular sampling of real space, a regular sampling of 3D orientation space is introduced (see Fig. 2 for an illustration of this concept). Each real space volume element (voxel) is assigned a finite set of discrete orientations which are used to model ("probe") the local orientation distribution of the grain. Using three position and three orientation space coordinates we operate in a six-dimensional position-orientation space: each of its elements holds a scalar quantity describing the volume fraction of material occupied by one of the sampled orientations at one of the sampled positions. Using such a description, the diffracted intensities $\mathbf{b}$ observed on the detector can be expressed by the action of a linear forward projection operator $\mathbf{A}$ on the set of unknown position-orientation space elements $\mathbf{x}$ as: $\mathbf{A} \times \mathbf{x} = \mathbf{b}$. As detailed in section 2 this equation represents a large-scale, system of linear equations. Approximate solutions can be found using iterative tomographic optimization schemes based on iterative forward and back-projection operations and exploiting prior knowledge (e.g. smoothness, non-negativity) about the

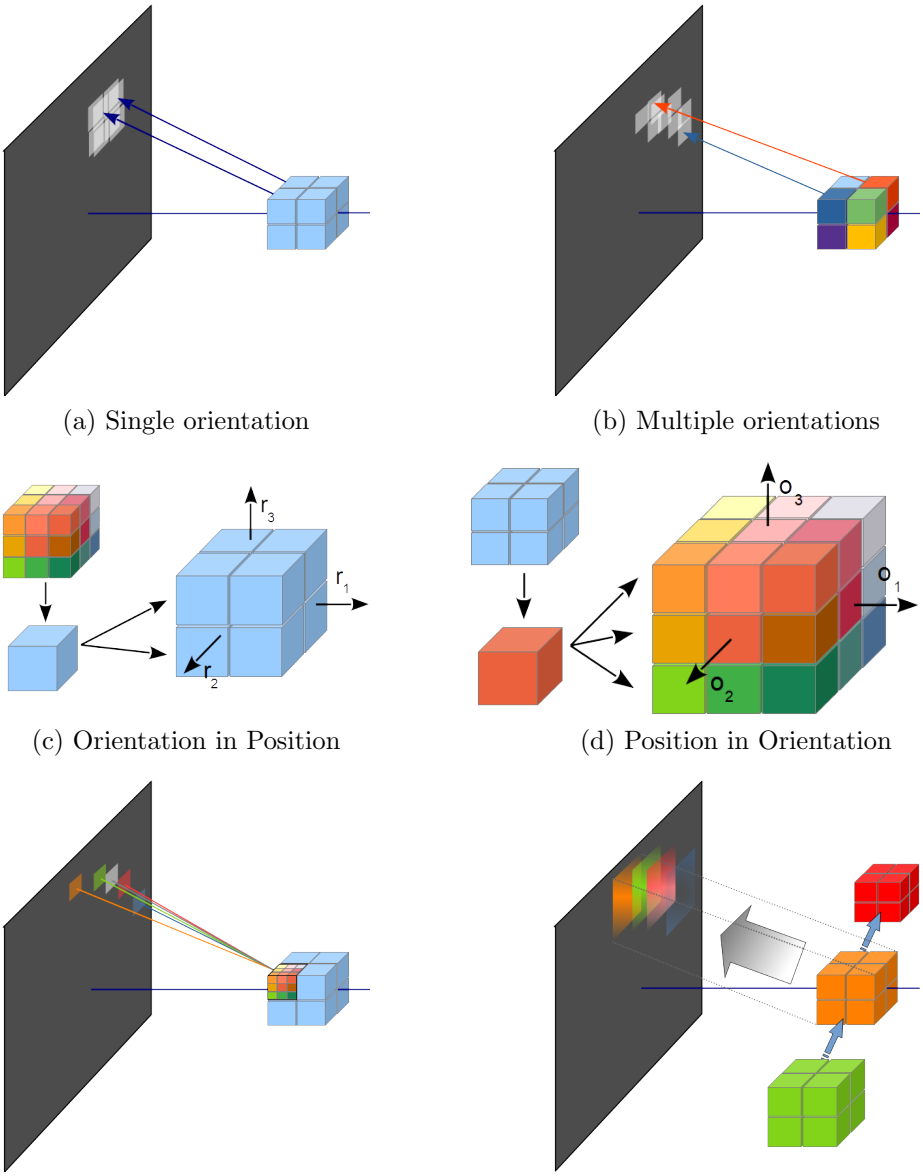

(a) Single orientation

(b) Multiple orientations

(c) Orientation in Position

(d) Position in Orientation

(e) Vector projector

(f) Series of 3D volume projections

Figure 2: (a) Parallel beam forward projection of a scalar volume for the case of a single (constant) orientation in 3D-DCT, (b) Distorted projection for the case of a deformed crystal, represented as a vector field - i.e. one distinct orientation for each real-space volume element. Different colors represent different orientations inside the grain volume. (c) Representation of the 6D position-orientation space as a collection of orientation sub-spaces (one per real-space element). The presence of an orientation distribution inside the voxel gives rise to azimuthal spread of intensity on the detector as illustrated in (e). (d) Alternative representation of the 6D position-orientation space as a collection of real-space volumes with distinct orientation. Our iterative reconstruction code uses this representation, in which case the forward projection corresponds to a cumulative sum of 3D volume projections as illustrated in (f). In both (c) and (d), the 6D 'voxels' hold a scalar quantity describing the "scattering power" of the element.

solution. A final processing step consists in converting the scalar 6D position-orientation output of the optimization algorithm back into a 3D vector field representation (e.g. 3 Euler angles) by calculating for each voxel the average of the 3D orientation distribution associated to it.

We now outline the structure of this article. In section 2 we present the generalized six-dimensional mathematical framework. In section 3 we present and compare the results obtained on a synthetic test case for which we have simulate selected combinations of low resolution and high resolution DCT and TT acquisitions. Some practical experimental aspects and limitations are discussed in section 4 before we conclude the article in section 5.

2. Method

In a typical diffraction imaging experiment, the investigated polycrystalline sample is placed on a diffractometer, while being irradiated by a monochromatic X-ray beam. The diffractometer allows to align the sample with a preferred orientation, and it incorporates a rotation stage which enables continuous rotations around a given axis over 2π. As the sample rotates, the Bragg condition is met by the different grains at specific angular positions ω, giving rise to diffracted beams. A high-resolution detector is usually positioned downstream the sample, and when it is intersected by the diffracted beams it records 3D diffraction "blobs" (i.e. 2D projection images showing parts of the diffracting grain, spread over a range of adjacent ω rotation angles).

2.1. Conventions

Each grain of the polycrystalline sample has an associated "crystal" coordinate system C_c, spanned by the orthogonal basis vectors: $C_\mathrm{c} = \{\mathbf{x}_\mathrm{c}, \mathbf{y}_\mathrm{c}, \mathbf{z}_\mathrm{c}\}$. The "laboratory" coordinate system C_l has the origin in the center of the sample, and it is defined by the right-handed orthogonal basis vectors: $C_\mathrm{l} = \{\mathbf{x}_\mathrm{l}, \mathbf{y}_\mathrm{l}, \mathbf{z}_\mathrm{l}\}$, where $\mathbf{x}_\mathrm{l}$ is oriented parallel to the incoming X-ray beam, $\mathbf{y}_\mathrm{l}$ lies in the horizontal plane, and $\mathbf{z}_\mathrm{l}$ is oriented vertically. The "sample" coordinate system C_s is oriented as the C_l coordinate system when no rotations are applied to diffractometer, aside from minor adjustments of the sample tilts. The two dimensional "detector" coordinate system is $C_\mathrm{d} = \{\mathbf{u}, \mathbf{v}\}$, where $\mathbf{u}$ is approximately parallel to $\mathbf{y}_l$, while $\mathbf{v}$ is approximately anti-parallel to $\mathbf{z}_l$.

2.2. Diffraction geometry

The unitary orientation matrix $\boldsymbol{g}$ defines the orientation of the crystal coordinate system with respect to the sample coordinate system. A given lattice plane normal $\mathbf{h}_\mathrm{c}$ in the crystal coordinates is expressed in sample coordinates as $\mathbf{h}_\mathrm{s} = \boldsymbol{g}^{-1}\mathbf{h}_\mathrm{c}$ (defined in Appendix A). The diffractometer transformation matrix $\boldsymbol{D}$ transforms the plane normal $\mathbf{h}_\mathrm{s}$ in laboratory coordinates $\mathbf{h}_\mathrm{l} = \boldsymbol{D}\mathbf{h}_\mathrm{s}$. Given an incoming monochromatic X-ray beam along the direction $\hat{\mathbf{b}}$, and a Bragg angle θ, we observe diffraction when the following expression is satisfied:

$$\hat{\mathbf{b}} \cdot \mathbf{h}_\mathrm{l} = \pm \sin\theta \,. \tag{1}$$

More details can be found in Appendix B. We define η as the angle between the following two lines over the detector: the projected sample rotation axis, and the projection of the scattering direction $\hat{\mathbf{d}}$.

The diffractometer transformation matrix $\boldsymbol{D}$ can be decomposed into rotation and translation components. As an example, for the setup on the beamline ID11 of the ESRF (The European Synchrotron, Grenoble, France), $\boldsymbol{D}$ is:

$$\boldsymbol{D} = \boldsymbol{\Phi}_\phi \boldsymbol{\Omega}_\omega \boldsymbol{R}_y \boldsymbol{R}_x \boldsymbol{T}_y \boldsymbol{T}_x \,, \tag{2}$$

where the stages from right to left are stacked in order from top to bottom. $\boldsymbol{T}_x$ and $\boldsymbol{T}_y$ are translations along the axes x and y respectively. $\boldsymbol{R}_x$ and $\boldsymbol{R}_y$ are tilts along the axes x and y respectively. $\boldsymbol{\Omega}_\omega$ is a rotation stage around the z-axis by the angle ω, and $\boldsymbol{\Phi}_\phi$ is another tilt around the y-axis by the angle ϕ, also known as "base-tilt" (Fig. 1). The positive direction of the related angles follows the right-hand rule with respect to the orientation of the related rotation axis, and the zero position is so that the sample coordinate system coincides with the laboratory coordinate system.

2.3. DCT

DCT experiments are specific instances of the geometry defined in section 2.2, with base-tilt $\phi = 0$ (Fig. 1a). The tilt stages $\boldsymbol{R}_x$ and $\boldsymbol{R}_y$ in equation (2) are used to align one of the sample's principal directions with the z-axis, which is commonly the rotation axis of the $\boldsymbol{\Omega}_\omega$ rotation stage. The translation stages $\boldsymbol{T}_x$ and $\boldsymbol{T}_y$ are used to bring sample center on the said z-axis. The angle ω spans the entire range from 0 to 2π. For more details we refer to [29].

As the sample rotates over the z-axis by the angle ω, the different grains reach diffraction condition, and give rise to diffracted beams, described by the tuple $(\omega, 2\theta, \eta)$. Correspondingly, at these ω angles we observe dimming of the direct beam in correspondence of the position of the diffracting grains. These shadows are called extinction spots.

Perfectly re-crystallized grains satisfy diffraction condition at precise ω and η positions. As they experience plastic deformation, different parts of the grain volumes undergo rotations of the underlying crystal lattice with respect to the average grain crystal orientation. These regions diffract at similar but different ω and η values, causing a broadening of the diffraction blobs, especially in ω. Diffracted beams intersecting the detector, can be alternatively parametrized by the tuple (ω, u, v), where (u, v) are pixel coordinates in the detector coordinate system C_{d}.

In usual DCT experiments, a high resolution detector, with pixel-sizes of $1-10\,\mu$m, is positioned at a distance of a few millimeters downstream the sample. This configuration is known as *near-field*, and it provides the 3D grain shape information. In the alternative configuration known as *far-field*, the detector is placed several centimeters from the sample, with pixel-sizes around $10 - 50$ times larger than in the near-field configuration. This configuration provides higher sensitivity to sub-grain level orientation changes, at the expense of spatial resolution.

2.4. Topo-tomography

TT experiments are also specific instances of the geometry defined in section 2.2 (Fig. 1b), and they allow to obtain significantly higher spatial resolution reconstructions of specific grains. The translation stages $\boldsymbol{T}_x$ and $\boldsymbol{T}_y$ are used to bring the center of the investigated grain on the z-axis. The tilt stages $\boldsymbol{R}_x$ and $\boldsymbol{R}_y$ are used to align a chosen grain plane normal with the rotation axis of the $\boldsymbol{\Omega}_\omega$ rotation stage (z-axis).

The angle ω spans the entire range from 0 to 2π, and the base-tilt ϕ spans an even range of a few degrees around the Bragg angle θ for the chosen plane normal. This allows to keep the same plane normal in diffraction condition at each ω, while having the grain center on the rotation axis eliminates (or strongly reduces) the precession of the diffracted beam. For more details we refer to [13].

Depending on the different local crystal orientation, different regions of the grain volume may diffract at different ϕ values in the scanned range. TT blobs can be parametrized by the tuple (ω, ϕ, η), where η is close to 0, or by the alternative parametrization (ω, ϕ, u, v).

2.5. Projection model

A six-dimensional model for the reconstruction of sub-grain crystal orientation from near-field DCT data was introduced in [27], and further developed in [28, 30]. It is based on [31], and it introduces a discrete sampling of the local orientation space centered around each grain average orientation. The grain reconstruction space $\mathbb{X}^6 = \mathbb{R}^3 \otimes \mathbb{O}^3$ is the outer product of the Cartesian position space and the three-dimensional Rodrigues orientation space $\mathbb{O}^3 \subseteq \mathbb{R}^3$ [32, 33]. This model neglects any elastic distortion of the crystal unit cell, which in the case of ductile metals is typically $\leq 1\%$. It also assumes kinematic diffraction and it neglects any physical correction, like photoelectric absorption and extinction effects. The position and orientation spaces of each reconstruction are defined along sample coordinates C_s. Thus, given the Rodriguez orientation coordinates system $C_\mathrm{o} = \{\mathbf{x}_\mathrm{o}, \mathbf{y}_\mathrm{o}, \mathbf{z}_\mathrm{o}\}$, displacements along the axes $\mathbf{x}_\mathrm{o}$, $\mathbf{y}_\mathrm{o}$, and $\mathbf{z}_\mathrm{o}$ identify rotations around the axis $\mathbf{x}_\mathrm{s}$, $\mathbf{y}_\mathrm{s}$, $\mathbf{z}_\mathrm{s}$, respectively.

In our six-dimensional model, the "forward projection" operation projects each of the 6D volume elements along its diffracted beam direction to the detector unit-areas (pixels). A graphical illustration of this projection operation and two alternative representations of the 6D position-orientation space are provided inFig. 2.

The adjoint operation is the "back-projection". They are derived in Appendix C, and they are defined respectively as:

$$B'_{(h,k,l)}(u, v, \phi, \omega) = \int_{\Omega_{\mathrm{R,O}}} X(\mathbf{r}, \mathbf{o})\, I(u, v, \phi, \omega, \mathbf{r}, \mathbf{o})\, C_{(h,k,l)}\, \mathrm{d}\mathbf{r}\mathrm{d}\mathbf{o}\,, \tag{3}$$

$$X'(\mathbf{r}, \mathbf{o}) = \int_{\Omega_\mathrm{D}} B_{(h,k,l)}(u, v, \phi, \omega)\, I(u, v, \phi, \omega, \mathbf{r}, \mathbf{o})\, C_{(h,k,l)}\, \mathrm{d}u\mathrm{d}v\mathrm{d}\phi\mathrm{d}\omega\,, \tag{4}$$

where the function $X(\mathbf{r}, \mathbf{o}) \in \mathcal{S}(\mathbb{R}^6) : \mathbb{X}^6 \mapsto [0, 1] \subset \mathbb{R}$ is a scalar six-dimensional function that gives the local mass fraction of the orientation $\mathbf{o}$ in the point $\mathbf{r}$, the constant $C_{(h,k,l)}$ is the scattering intensity per unit volume of the lattice plane (h, k, l) and given material, $B'_{(h,k,l)}(u, v, \omega) \in \mathcal{S}(\mathbb{R}^3) : \mathbb{R}^3 \mapsto \mathbb{R}$ is the

scalar three-dimensional function representing the produced blob, and $\Omega_{\mathrm{R,O}}$ is the support of the function $X(\mathbf{r}, \mathbf{o})$ in the $\mathbb{X}^6 = \mathbb{R}^3 \otimes \mathbb{O}^3$ reconstruction space.

If we suppose that in each position-space point, only one orientation is active, we can compress the six-dimensional scalar function $X(\mathbf{r}, \mathbf{o}) \in \mathcal{S}(\mathbb{R}^6) : \mathbb{X}^6 \mapsto \mathbb{R}$ into a three-dimensional four-components vector function $\mathbf{X}(\mathbf{r}) \in \mathcal{V}_4(\mathbb{R}^3) : \mathbb{R}^3 \mapsto \mathbb{R}^4$. Its most straight-forward representation is given by the local mass fraction $f \in \mathcal{S}(\mathbb{R}^3) : \mathbb{R}^3 \mapsto [0, 1] \subset \mathbb{R}$ as zeroth component, and the active orientation $\mathbf{o}$ as the remaining three components. Transformations allowing to obtain and work with this representation are presented in Appendix D.

2.6. Reconstruction formulation

Each sampled point in the orientation space has a fixed projection geometry. If we discretize the position-orientation space and the detector positions (u, b, ϕ, ω), equation (3) becomes:

$$B'_{(h,k,l)}(u, v, \phi, \omega) = \sum_{i=0}^{R} \sum_{j=0}^{P} X(r_i, o_p)\, I(u, v, \phi, \omega, r_i, o_p)\, C_{(h,k,l)}\,, \tag{5}$$

where R and P are the total number of sampled points in position and orientation space, respectively. The matrix representation of equation (5) is:

$$\mathbf{b}_m = \begin{pmatrix} \boldsymbol{A}_{m1} & \boldsymbol{A}_{m2} & \cdots & \boldsymbol{A}_{mP} \end{pmatrix} \begin{pmatrix} \mathbf{x}_1 \\ \mathbf{x}_2 \\ \vdots \\ \mathbf{x}_P \end{pmatrix}, \tag{6}$$

where the index m indicates the given blob, the vector $\mathbf{b}_m$ is its discretization, the vectors $\mathbf{x}_p$, with $p \in [1, P] \subset \mathbb{N}$, are the three-dimensional volumes associated to each sampled orientation, and the corresponding matrices $\boldsymbol{A}_{mp}$ are the projection matrices for the given blob m and orientation p. The collection of projection matrices $\boldsymbol{A}_{mp}$ for a fixed m is the discretization of the integral forward projection operator $\mathbb{A}_{(h,k,l)}$. The transpose of this collection is the discretization of the integral back-projection operator $\mathbb{A}^{\dagger}_{(h,k,l)}$ from Appendix C. Given M total acquired diffraction blobs for a given grain in a generic acquisition

scheme, the resulting forward model is:

$$\mathbf{b} = \begin{pmatrix} \mathbf{b}_1 \\ \mathbf{b}_2 \\ \vdots \\ \mathbf{b}_M \end{pmatrix} = \begin{pmatrix} \boldsymbol{A}_{11} & \cdots & \boldsymbol{A}_{1P} \\ \vdots & \ddots & \vdots \\ \boldsymbol{A}_{M1} & \cdots & \boldsymbol{A}_{MP} \end{pmatrix} \begin{pmatrix} \mathbf{x}_1 \\ \mathbf{x}_2 \\ \vdots \\ \mathbf{x}_P \end{pmatrix}, \tag{7}$$

where the vectors $\mathbf{b}_m$, with $m \in [1, M] \subset \mathbb{N}$, form the collection of all the recorded blobs.

In [27] we proposed to solve the inverse problem in equation (7) by minimizing the l_2-norm of the residual over the detector:

$$\begin{aligned} \mathbf{x}^* = \underset{\mathbf{x}}{\operatorname{argmin}} \left\{ ||\boldsymbol{A}\mathbf{x} - \mathbf{b}||_2^2 + \lambda || \left(\boldsymbol{O}\mathbf{x}\right) ||_1 \right\} \\ \text{subject to: } \mathbf{x} \geq \mathbf{0}\,, \end{aligned} \tag{8}$$

where the operator $\boldsymbol{O}$ produces a representation in which we know *a priori* that the expected reconstruction has a sparse representation. Popular choices for the operator $\boldsymbol{O}$ are the Total Variation [34] and the wavelet transform [35]. For the solution of equation (8) many algorithms can be used, including: established interior-point methods [36], and more recent approaches like Chambolle-Pock [37]. Due to the generality of equation (7), the formulation in equation (8) is trivially applicable to both DCT and TT reconstructions.

This can be generalized to:

$$\begin{aligned} \mathbf{x}^* = \underset{\mathbf{x}}{\operatorname{argmin}} \left\{ \sum_i \gamma_i ||\boldsymbol{A}_i\mathbf{x} - \mathbf{b}_i||_2^2 + \lambda || \left(\boldsymbol{O}\mathbf{x}\right) ||_1 \right\} \\ \text{subject to: } \mathbf{x} \geq \mathbf{0}\,, \end{aligned} \tag{9}$$

where the values γ_i are weighting factors, and i is the index of the considered acquisition. This allows to use multiple types of acquisitions, including: near-field and far-field DCT, and TT acquisitions.

3. Numerical examples

We now show the application of the method introduced in section 2 for a single grain. We use synthetic data because it allows to test the reconstruction performance against the known ground truth. The results obtained on a single

grain are representative for polycrystalline sample volumes provided diffraction spot overlap on the detector remains limited.

3.1. Data description

We present a single-grain reconstruction, where the simulated material is Ti (hcp unit-cell), and the grain has cubic shape. The size of the simulated grain is $50\,\mu\text{m} \times 50\,\mu\text{m} \times 50\,\mu\text{m}$, divided in $250 \times 250 \times 250$ cubic unit-volumes (voxels) with edge sizes of $0.2\mu\text{m}$. The orientation-space bounding box of the grain orientation distribution function (ODF) is $0.489° \times 0.506° \times 0.514°$ large, with a maximum orientation spread of $0.8°$. The deformation presents itself in the form of mosaicity and small-scale variations, with some strong deformation gradients close to the sub-grain boundaries. For more details on the synthetic grain we refer to Appendix F. The ground truth is defined using the vector representation discussed in section 2.5, and the diffraction images are simulated using a discrete implementation of equation (D.3), which was derived in Appendix C. Each reconstruction is also projected onto the vector representation, for comparison against the ground truth.

We generated three different types of acquisitions for an incoming beam of energy equal to 36 keV: [A] a DCT acquisition, with a flat detector at 10 mm from the sample and 2.5 μm pixel-size; [B] a TT acquisition on the [0 0 0 2] lattice plane, with a flat detector at 6 mm from the sample, and 0.75 μm pixel-size; [C] a DCT acquisition on a flat detector at 6 mm from the sample and 0.75 μm pixel-size, with a lateral displacement that allowed to image only the reflections on one side of the sample. All the DCT acquisitions use steps in ω of 0.1 degrees, while the TT acquisition has base-tilt range $[-6, -2]$ degrees in steps of 0.05 degrees, and steps in ω of 4 degrees. For acquisition [A] we only used 60 diffraction blobs, out of its 96 falling onto the 2048×2048 pixels detector, while for acquisition [C] we used all the 30 blobs falling on the detector. For acquisition [B] we used all the 90 blobs resulting from a 360 degrees scan.

The reconstructions were performed at 0.05 degrees orientation-space resolution, using the 6D Chambolle-Pock isotropic TV-min implementation from [38], already used in [39], with weight $\lambda = 1 \times 10^{-4}$, and 100 iterations.

To analyze and compare the performance of the different reconstructions we use the same slice in the XY plane of the grain 3D position-space volume.

This slice is close to the central slice of the volume, and it was chosen because it presents multiple sub-grains. For the said slice we present the shape of the reconstructed intensity profile, and the local orientation space reconstruction error against the ground truth.

3.2. TT orientation reconstruction

We first apply the method described in section 2 to the reconstruction of TT data from deformed grains. This allows the extension of existing 3-dimensional reconstruction techniques, for increasing grain deformation. TT acquisitions are not sensitive to the orientation components parallel to the lattice plane aligned with the rotation axis (for more information refer to Appendix E). Thus, TT reconstructions are intrinsically 5-dimensional (3D position-space plus 2D orientation-space), because their data only allows to reconstruct orientation variations along such plane.

Figure 3 shows that for this example, the traditional 3D reconstruction methods provide an incorrect reconstruction, while the presented method retrieves the overall grain shape correctly. The red line in Fig. 3 indicates the expected grain boundary from automatic segmentation of the phantom, while the the green line defines the actually segmented grain boundary from the reconstructed volume. Concerning the grain shape reconstruction for the presented method, only the grain boundaries with abrupt changes in orientation provide a decrease in reconstruction quality and accuracy. This is confirmed by Fig. 3(d), where the local orientation reconstruction error (in the XY orientation components) is plotted: The grain boundaries present the highest reconstruction error. The effect of the TT insensitivity to orientation changes along the selected plane normal is clearly visible in Fig. 3(e). There the local 3D orientation (XYZ in orientation-space) reconstruction error is plotted, and it shows much larger deviations than in Fig. 3(e).

3.3. Combining DCT and TT

TT acquisitions allow high-resolution position and orientation-space information to be acquired, but lack the ability to index grains or probe the orientation space component parallel to the sample rotation axis. DCT acquisitions

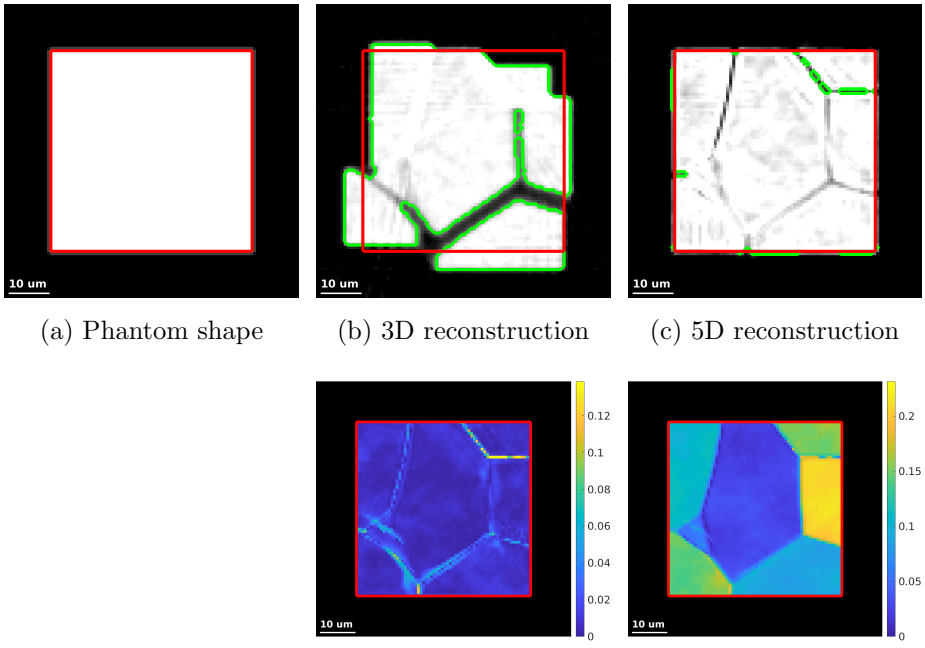

(a) Phantom shape (b) 3D reconstruction (c) 5D reconstruction

(d) 2D orientation error (e) 3D orientation error

Figure 3: Reconstruction of TT data of the deformed grains using our method: (a) Phantom; (b) Single orientation, 3D TT reconstruction (3D position-space); (c) 0.05 orientation space resolution 5D TT reconstruction (3D position-space + 2D orientation-space); (d) Local orientation reconstruction error for (c) in the orientation XY plane; (e) Local orientation reconstruction error for (c) with respect to the full orientation space. The largest component of the error in (e) is due to the inability of TT to probe orientation changes along the chosen lattice plane normal (in this case, parallel to the sample z-axis). (d) is the projection of (e) on the 2D orientation-space of the reconstruction. The red line is the expected grain profile from the segmentation of the phantom, while the green line is the actual profile from the segmentation of the reconstruction

.

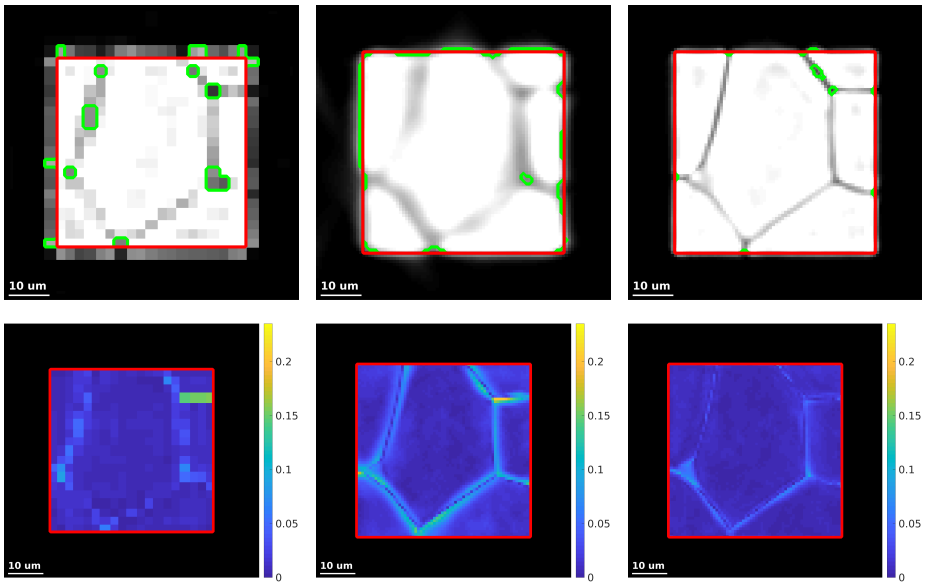

(a) [A] at 2.5 μm (b) [A] at 0.75 μm (c) [A B] at 0.75 μm

Figure 4: Comparison of reconstruction performance at different position-space resolutions for different setup configurations. The top row shows grain shape reconstructions, while the bottom row shows the corresponding local orientation reconstruction error. The columns are: (a) DCT [A] with 60 blobs acquired at 2.5 μm pixel-size, reconstructed at 2.5 μm voxel size; (b) DCT [A] with 60 blobs acquired at 2.5 μm pixel-size, reconstructed at 0.75 μm voxel size; (c) DCT [A] with 60 blobs acquired at 2.5 μm pixel-size and TT [B] with 90 blobs acquired at 0.75 μm pixel-size, reconstructed at 0.75 μm voxel size.

present complementary characteristics to TT acquisitions. Moreover, DCT offers higher sensitivity to deformations along the z-axis, and TT higher sensitivity on the plane parallel to the selected plane normal, which is usually close to the sample XY-plane (for more information we refer to Appendix E). This renders them a perfect match for the multi-modal reconstructions made possible by the method presented in this article.

Figure 4 demonstrates that by combining DCT acquisitions with higher resolution TT acquisitions, it is possible to obtain a high resolution grain reconstruction in both spatial and orientation components. The first column in Fig. 4 presents the low resolution DCT acquisition [A] reconstructed at its native 2.5 μm voxel-size. The second column presents the reconstruction of the same dataset at a markedly higher position-space resolution of 0.75 μm voxel-size. From its shape reconstruction in the top row, we see that the reconstruction

is blurred. This is reflected in the corresponding local orientation error map, which shows that it fails to accurately reconstruct the local orientation, especially at sub-grain boundary regions. In Fig. 4(c) we see that by joining the low resolution DCT acquisition [A] with the 0.75 μm pixel-size TT acquisition [B], we obtain a much higher resolution reconstruction both in position and orientation space.

3.4. Combining DCT scans of different pixel-size

While the previous example shows that TT acquisitions can be used to greatly enhance DCT resolution and accuracy, it is not possible to perform TT acquisitions for all the grains in a dataset during a single experiment, when a sample contains thousands of grains. The presented method however, allows to complement low resolution DCT acquisitions with diffraction blobs from high resolution DCT acquisitions. The collected high resolution blobs from a high resolution DCT acquisition would be much fewer in a typical TT acquisition. They would however be able to offer the same spatial resolution, and for all the grains in a single additional acquisition.

Figure 5, similarly to Fig. 4, compares reconstructions from just the low resolution DCT acquisition [A], at 2.5 and 0.75 μm position-space resolutions against the combined low resolution [A] and high resolution [C] DCT acquisitions. While the improvement for the configuration [A C] over the reconstruction only using low resolution data is less substantial than in the [A B] configuration (low resolution DCT combined with TT), it is visible and measurable. This can be seen both in the shape reconstruction in the top row of Fig. 5(c), and in the corresponding local orientation reconstruction error in the bottom row.

3.5. Performance quantification

The observations obtained from the reconstructions presented in the previous two sections are supported by the error histogram plots of the whole reconstructed volume. Figure 6 shows the comparison between the reconstruction error histograms of the following three configurations: [A] DCT acquisition at 2.5 μm, [AB] DCT acquisition at 2.5 μm combined with TT acquisition at 0.75 μm, [AC] DCT acquisition at 2.5 μm combined with DCT acquisition at 0.75 μm, all reconstructed at 0.75 μm. While for the first configuration the average

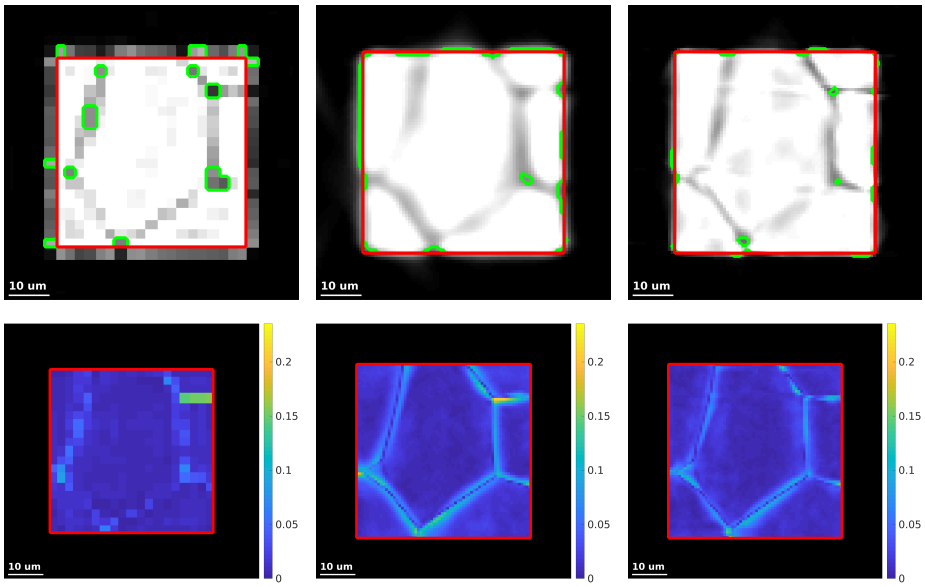

(a) [A] at 2.5 μm (b) [A] at 0.75 μm (c) [A C] at 0.75 μm

Figure 5: Comparison of reconstruction performance at different position-space resolutions for different setup configurations. The top row shows grain shape reconstructions, while the bottom row shows the corresponding local orientation reconstruction error. The columns are: (a) DCT [A] with 60 blobs acquired at 2.5 μm pixel-size, reconstructed at 2.5 μm voxel size; (b) DCT [A] with 60 blobs acquired at 2.5 μm pixel-size, reconstructed at 0.75 μm voxel size; (c) DCT [A] with 60 blobs acquired at 2.5 μm pixel-size and DCT [C] with 30 blobs acquired at 0.75 μm pixel-size, reconstructed at 0.75 μm voxel size.

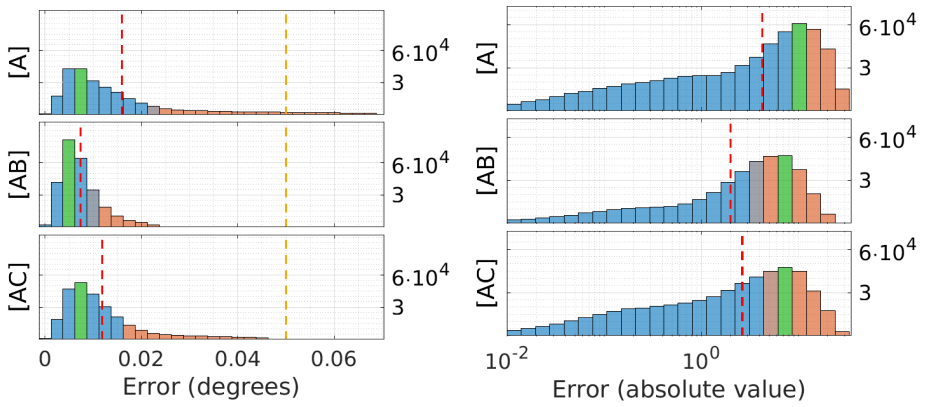

(a) Orientation (b) Intensity

Figure 6: Local reconstruction error histograms for: (a) Orientation (linear scale); (b) Intensity (logarithmic scale). The red line marks the distribution mean value, the orange histograms the upper 20 percentile of the distribution, and the green histogram the mode of the distribution. In (a) the orange line marks the orientation-space reconstruction resolution. The three configurations correspond to: [A] DCT acquisition at 2.5 μm, [AB] DCT acquisition at 2.5 μm combined with TT acquisition at 0.75 μm, [AC] DCT acquisition at 2.5 μm combined with DCT acquisition at 0.75 μm, respectively.

local orientation reconstruction error is 0.016 degrees, for the second and the third it decreases to 0.0075 and 0.012 degrees respectively.

The local material concentration is the material mass fraction multiplied by its density and the single voxel volume. Its reconstruction accuracy is represented by the local reconstructed total intensity through-out all the sampled orientations. The first configuration is affected by an average error of 4.233 over an expected intensity of $\sim$ 52.734, while the second and third are affected by average deviations of 1.998 and 2.641 respectively.

These plots confirm that the coupling of low spatial resolution DCT with high resolution TT or DCT can significantly increase both the orientation-space and position-space reconstruction accuracy. Moreover, from Fig. 6 we can clearly notice a strong reduction on the outliers of the distributions.

The reconstruction resolution can be estimated as the size of the blur kernel that when convolved with the phantom has the least difference from the reconstruction. This estimation assumes perfect reconstructions (artifact free), and it is inherently an approximation. Here we assume sphere type of blur because the detector images are not affected by a point spread function. For the presented

three configurations [A], [A B], and [A C], we obtained blur radii of: 4.48, 1.71, and 2.74 pixels respectively.

4. Discussion

4.1. Experimental considerations

The combined acquisition schemes proposed in the current article involve experiments with two different effective pixel sizes. Detector systems featuring a motorized microscope objective turret offer the possibility to integrate such remote control changes of the optical configuration into fully automated scanning sequences without need for human intervention. In the case of TT, the centering of the grain of interest on the rotation axis not only leads to the stationary position of the diffracted beam, required for the deployment of a high resolution detector system, but also allows for a significant reduction of the scan times, since the incoming X-ray beam can be condensed onto the projected area of the grain. In the case of ID11 this type of dynamic focusing can be achieved using a modular system of compound refractive lenses, also known as X-ray transfocator [40]. Although in our simulation the combination of DCT and TT show the biggest improvement in terms of spatial resolution and orientation error, practical limitations may arise from the limited sample goniometer tilt range and diffractometer error motion. With typical sample tilt ranges of order of $\pm 20^\circ$ it may not be possible to align one of the low index reflections for unfavourably oriented grains. Similarly, in order to obtain a spatial resolution comparable to the detector pixel size the mechanical error motion of the scanned diffractometer axis has to be of the same order as the pixel size. While this condition is usually fulfilled for modern airbearing rotation stages deployed in tomographic imaging applications, it may not hold for all of the axes of conventional diffractometers. Correction schemes based on a look-up table for the reproducible part of this error motion and additional optimization schemes for projection re-alignment may thus be required to reach the ultimate resolution.

The framework introduced in this article can be applied to other combinations of acquisitions, including high resolution DCT scans at different energy and/or sample tilt settings to compensate for the limited number of diffraction spots intercepted by the detector. Alternatively, TT acquisition from several

scattering vectors and/or at different sample to detector distances can be combined to further increase the sensitivity and to push the spatial resolution of this technique towards the limits set by current detector technology.

4.2. Data collection efficiency and limitations

The proposed combination(s) of low resolution and high resolution DCT and TT scans are based on fast (extended beam, single axis) continuous scan acquisitions and for that reason highly time efficient. Further optimization of time efficiency can be achieved using a 3D detector concept based on two semi-transparent scintillator screens placed at different distance and enabling simultaneous acquisition of projection images with a different effective pixel size, as proposed by Poulsen and co-workers [41]. The use of such a system suppresses the need for a second acquisition and would be ideally suited for (non-interrupted) in-situ observations on slowly evolving 3D microstructures.

We further emphasize that extended beam acquisition schemes intrinsically provide isotroptic voxel-resolution in three dimensions as opposed to slice beam acquisition schemes, which often use a coarser step size in the stacking direction in order to reduce the overall acquisition time when scanning extended 3D sample volumes. On the other hand, the full-field approaches described in this study are subject to the known limitations inherent to diffraction spot segmentation and indexing based, inverse reconstruction schemes. Compared to forward modeling based reconstruction [19], more stringent restrictions apply on the maximum number of simultaneously illuminated grains in the sample volume, the maximum acceptable intragranular orientation spread and sample texture (see [29]).

5. Conclusions and outlook

The work presented in this article introduces a generalization of tomographic reconstruction algorithms for 3D orientation mapping in polycrystalline materials. The generalized reconstruction scheme can handle arbitrary combinations of projection data, stemming from acquisitions with different detector pixel size and sample tilt settings. With the introduction of appropriate diffractometer

transformation matrices, the scattering geometry for acquisitions around different diffractometer axis can be unified and described in a common sample reference frame. The reconstruction of the orientation field is based on the assumption of kinematic diffraction and uses an iterative optimization algorithm, minimizing the projection distance between the current solution and the observed diffraction intensities recorded on the detector [30]. As demonstrated on synthetic test data, the combination of a limited amount of high spatial resolution projections (i.e. limited data from rotation around a single scattering vector like in TT, or a limited amount of low index reflections from a high resolution DCT scan) and conventional DCT data (acquired at the appropriate detector resolution to cover the innermost 3-5 *hkl* families) result in a measurable improvement of the reconstruction quality compared to the individual acquisitions. The sequential combination of two fast (full-field) acquisitions offers a time efficient alternative to other 3DXRD techniques based on two and three-dimensional scanning schemes. Concerning potential applications we highlight two scientific areas where the increased spatial and angular resolution could be particularly beneficial: (1) time-lapse studies of curvature driven grain coarsening require access to accurate grain boundary positions and will benefit from the combination of low resolution and high resolution DCT acquisitions; (2) studies of strain localization and propagation of plasticity throughout a polycrystalline microstructure require ultimate spatial and angular resolution in order to capture subtle variations of the orientation field in vicinity of slip bands. The proposed combination of DCT and TT may enable in-situ observation of early stages of plastic deformation in the bulk of polycrystalline sample volumes. The generalized diffraction geometry introduced in this work can be readily extended to other diffraction imaging techniques (laboratory X-rays, neutrons, X-ray Dark Field Microscopy) and may also prove beneficial for forward modeling based reconstruction schemes [19].

6. Acknowledgments

NV acknowledges support from the European Union's Horizon 2020 research and innovation programme (VOXEL H2020-FETOPEN-2014-2015-RIA GA 665207).

NV acknowledges support from the NVIDIA Corporation, through their GPU Grant Program, and the associated donation of a TITAN Xp card.

Appendix A. Basis vectors

Given a three-dimensional crystal lattice described by the basis vectors $\mathbf{a}$, $\mathbf{b}$ and $\mathbf{c}$, defined in the crystal coordinate system C_c, the crystal unit cell is the minimal space spanned by these vectors. The vectors $\mathbf{a}^*$, $\mathbf{b}^*$ and $\mathbf{c}^*$, are the reciprocal vectors of $\mathbf{a}$, $\mathbf{b}$ and $\mathbf{c}$. The space spanned by the vectors $\mathbf{a}^*$, $\mathbf{b}^*$ and $\mathbf{c}^*$ is called reciprocal (Fourier) space, and they define the se-called reciprocal lattice [42].

Diffraction is observed when the difference between an incoming X-ray beam wave-vector $\mathbf{k}_\mathrm{in}$ and an observed outgoing X-ray wave-vector $\mathbf{k}_\mathrm{out}$ is close to a point on the reciprocal lattice. This means that $\mathbf{h}_\mathrm{hkl} = \mathbf{k}_\mathrm{in} - \mathbf{k}_\mathrm{out}$ and that $\mathbf{h}_\mathrm{hkl} = (h\mathbf{a}^*, k\mathbf{b}^*, l\mathbf{c}^*)^T$, where $h, k, l \in \mathbb{Z}$ are the Miller indexes. The lattice plane corresponding to the vector $\mathbf{h}_\mathrm{hkl}$ is identified by the plane normal $\mathbf{h}_\mathrm{c} = \boldsymbol{B}\mathbf{h}_\mathrm{hkl}$. The matrix B is an upper triangular matrix that transforms vectors from reciprocal space into vectors of the real space. More details can be found in [43].

Appendix B. Diffraction conditions

For a given lattice plane normal $\mathbf{h}_\mathrm{c}$ in the crystal coordinates, it is expressed in sample coordinates as $\mathbf{h}_\mathrm{s} = \boldsymbol{g}^{-1}\mathbf{h}_\mathrm{c}$. The diffractometer transformation matrix $\boldsymbol{D}$ transforms the plane normal $\mathbf{h}_\mathrm{s}$ in laboratory coordinates $\mathbf{h}_\mathrm{l} = \boldsymbol{D}\mathbf{h}_\mathrm{s}$. Given an incoming monochromatic X-ray beam along the direction of the vector $\hat{\mathbf{b}}$, and a Bragg angle θ, we observe diffraction when the following expression is satisfied:

$$\hat{\mathbf{b}} \cdot \mathbf{h}_\mathrm{l} = \hat{\mathbf{b}}^T \boldsymbol{D}\boldsymbol{g}^{-1}\boldsymbol{B} \begin{pmatrix} h \\ k \\ l \end{pmatrix} = \pm \sin\theta \,. \tag{B.1}$$

The observed diffracted beam is defined through the parallelogram law of vector addition as $\hat{\mathbf{d}} = \hat{\mathbf{b}} + 2\mathbf{h}_\mathrm{l}(\hat{\mathbf{b}}^T\mathbf{h}_\mathrm{l})$.

The vectors $\mathbf{h}_\mathrm{l}$ and $\hat{\mathbf{d}}$ can be re-written in terms of the angles (θ, η):

$$\mathbf{h}_\mathrm{l} = \begin{pmatrix} -\cos\theta\tan\theta \\ -\cos\theta\sin\eta \\ \cos\theta\cos\eta \end{pmatrix}, \ \hat{\mathbf{d}} = \begin{pmatrix} \cos 2\theta \\ -\sin 2\theta\sin\eta \\ \cos 2\theta\cos\eta \end{pmatrix}, \tag{B.2}$$

where 2θ is the angle between $\hat{\mathbf{b}}$ and $\hat{\mathbf{d}}$, and $\hat{\mathbf{b}} = (1,0,0)^T$.

Appendix C. Derivation of projection equations

We define the center of detector coordinates in the laboratory coordinate system by the vector $\mathbf{s}_\mathrm{l}$, so that a given the position in detector coordinates (u, v) is equal to the following in laboratory coordinates:

$$\mathbf{p}_\mathrm{l}(u,v) = \mathbf{s}_\mathrm{l} + \begin{pmatrix} \mathbf{u} & \mathbf{v} \end{pmatrix} \begin{pmatrix} u \\ v \end{pmatrix}. \tag{C.1}$$

In DCT reconstructions, grain are conveniently reconstructed in sample coordinates, and have origin in the grain center, The given detector pixel position (u, v) in sample coordinates for a given ω is:

$$\mathbf{p}_\mathrm{s}(u,v,\omega) = \boldsymbol{D}_\mathrm{DCT}^{-1}(\omega)\cdot\mathbf{p}_\mathrm{l} - \mathbf{c}_\mathrm{s}\,, \tag{C.2}$$

where $\mathbf{c}_\mathrm{s}$ is the grain center in sample coordinates, and the diffractometer transformation $\boldsymbol{D}_\mathrm{DCT}$ is a function of ω. The direction of the scattered beam $\hat{\mathbf{d}}_{(h,k,l),\mathrm{l}}$, abbreviated to $\hat{\mathbf{d}}_\mathrm{l}$ for convenience, is a function of the local crystal lattice orientation $\mathbf{o}$:

$$\hat{\mathbf{d}}_\mathrm{l}(\omega,\mathbf{o}) = \hat{\mathbf{b}}_\mathrm{l} + 2\left(\hat{\mathbf{b}}_\mathrm{l}^T\cdot\mathbf{h}_\mathrm{l}(\omega,\mathbf{o})\right)\mathbf{h}_\mathrm{l}(\omega,\mathbf{o})\,, \tag{C.3}$$

where $\mathbf{h}_\mathrm{l}(\omega,\mathbf{o}) = \boldsymbol{D}_\mathrm{DCT}(\omega)\cdot\mathbf{h}_\mathrm{s}(\mathbf{o})$. The scattered beam direction $\hat{\mathbf{d}}_\mathrm{s}(\omega,\mathbf{o})$ in sample coordinates is:

$$\begin{aligned}
\hat{\mathbf{d}}_\mathrm{s}(\omega,\mathbf{o}) &= \boldsymbol{D}_\mathrm{DCT}^{-1}(\omega)\cdot\hat{\mathbf{d}}_\mathrm{l}(\omega,\mathbf{o}) \\
&= \boldsymbol{D}_\mathrm{DCT}^{-1}(\omega)\cdot\left(\hat{\mathbf{b}}_\mathrm{l} + 2\left(\hat{\mathbf{b}}_\mathrm{l}^T\cdot\boldsymbol{D}_\mathrm{DCT}(\omega)\cdot\mathbf{h}_\mathrm{s}(\mathbf{o})\right)\boldsymbol{D}_\mathrm{DCT}(\omega)\cdot\mathbf{h}_\mathrm{s}(\mathbf{o})\right) \\
&= \boldsymbol{D}_\mathrm{DCT}^{-1}(\omega)\cdot\hat{\mathbf{b}}_\mathrm{l} + 2\left(\left(\boldsymbol{D}_\mathrm{DCT}^{-1}(\omega)\cdot\hat{\mathbf{b}}_\mathrm{l}\right)^T\cdot\mathbf{h}_\mathrm{s}(\mathbf{o})\right)\mathbf{h}_\mathrm{s}(\mathbf{o}) \\
&= \hat{\mathbf{b}}_\mathrm{s}(\omega) + 2\left(\hat{\mathbf{b}}_\mathrm{s}(\omega)^T\cdot\mathbf{h}_\mathrm{s}(\mathbf{o})\right)\mathbf{h}_\mathrm{s}(\mathbf{o})\,,
\end{aligned} \tag{C.4}$$

where $\hat{\mathbf{b}}_{\mathrm{s}}(\omega) = \boldsymbol{D}^{-1}_{\mathrm{DCT}}(\omega)\hat{\mathbf{b}}_{\mathrm{l}}$.

If we now define the detector pixel position (u, v) with respect to a certain position in the grain volume $\mathbf{r}$, as $\mathbf{p}_{\mathrm{s}}(u, v, \omega, \mathbf{r}) = \mathbf{p}_{\mathrm{s}}(u, v, \omega) - \mathbf{r}$, we can define the DCT intensity deposition function in the point (u, v) of the detector from a point $\mathbf{r}$ in the grain volume, with orientation $\mathbf{o}$, as:

$$I(u, v, \omega, \mathbf{r}, \mathbf{o}) = \delta\left(\mathbf{p}_{\mathrm{s}}(u, v, \omega, \mathbf{r}) - \hat{\mathbf{d}}_{\mathrm{s}}(\omega, \mathbf{o})\left(\mathbf{p}_{\mathrm{s}}(u, v, \omega, \mathbf{r})^T \cdot \hat{\mathbf{d}}_{\mathrm{s}}(\omega, \mathbf{o})\right)\right), \quad \text{(C.5)}$$

where the function $\delta(\cdot)$ is Dirac delta. Using equation (C.5), the intensity deposition in the detector pixel (u, v, ω) from the whole grain volume, with respect to the sampled region of the orientation space, is:

$$\begin{aligned} B'_{(h,k,l)}(u, v, \omega) &= \int_{\Omega_{\mathrm{R,O}}} I(u, v, \omega, \mathbf{r}, \mathbf{o})\, X(\mathbf{r}, \mathbf{o})\, C_{(h,k,l)}\, \mathrm{d}\mathbf{r}\mathrm{d}\mathbf{o} \\ &= \int_{\Omega_{\mathrm{R,O}}} \delta\left(\mathbf{p}_{\mathrm{s}}(u, v, \omega, \mathbf{r}) - \hat{\mathbf{d}}_{\mathrm{s}}(\omega, \mathbf{o})\left(\mathbf{p}_{\mathrm{s}}(u, v, \omega, \mathbf{r})^T \cdot \hat{\mathbf{d}}_{\mathrm{s}}(\omega, \mathbf{o})\right)\right) \\ &\quad \times X(\mathbf{r}, \mathbf{o})\, C_{(h,k,l)}\, \mathrm{d}\mathbf{r}\mathrm{d}\mathbf{o}\,, \end{aligned} \quad \text{(C.6)}$$

where the function $X(\mathbf{r}, \mathbf{o}) \in \mathcal{S}(\mathbb{R}^6) : \mathbb{X}^6 \mapsto [0, 1] \subset \mathbb{R}$ is a scalar six-dimensional function that gives the local mass fraction of the orientation $\mathbf{o}$ in the point $\mathbf{r}$, the constant $C_{(h,k,l)}$ is the scattering intensity per unit volume of the lattice plane (h, k, l) and given material, $B'_{(h,k,l)}(u, v, \omega) \in \mathcal{S}(\mathbb{R}^3) : \mathbb{R}^3 \mapsto \mathbb{R}$ is the scalar three-dimensional function representing the produced blob, and $\Omega_{\mathrm{R,O}}$ is the support of the function $X(\mathbf{r}, \mathbf{o})$ in the $\mathbb{X}^6 = \mathbb{R}^3 \otimes \mathbb{O}^3$ reconstruction space.

The corresponding back-projection operation to the forward projection in equation (C.6), for the given point $\mathbf{r}$ and orientation $\mathbf{o}$ from the blob $B_{(h,k,l)}(u, v, \omega)$ can be defined as:

$$\begin{aligned} X'(\mathbf{r}, \mathbf{o}) &= \int_{\Omega_{\mathrm{D}}} I(u, v, \omega, \mathbf{r}, \mathbf{o})\, B_{(h,k,l)}(u, v, \omega)\, C_{(h,k,l)}\, \mathrm{d}u\mathrm{d}v\mathrm{d}\omega \\ &= \int_{\Omega_{\mathrm{D}}} \delta\left(\mathbf{p}_{\mathrm{s}}(u, v, \omega, \mathbf{r}) - \hat{\mathbf{d}}_{\mathrm{s}}(\omega, \mathbf{o})\left(\mathbf{p}_{\mathrm{s}}(u, v, \omega, \mathbf{r})^T \cdot \hat{\mathbf{d}}_{\mathrm{s}}(\omega, \mathbf{o})\right)\right) \\ &\quad \times B_{(h,k,l)}(u, v, \omega)\, C_{(h,k,l)}\, \mathrm{d}u\mathrm{d}v\mathrm{d}\omega\,, \end{aligned} \quad \text{(C.7)}$$

where now $X'(\mathbf{r}, \mathbf{o})$ is the back-projected intensity, and Ω_{D} is the support of the blob function $B(u, v, \omega)_{(h,k,l)}$.

Equations (C.6) and (C.7) can be further generalized, by considering them as the application of the integral forward-projection operator $\mathbb{A}_{\mathrm{DCT},(h,k,l)}\left[\cdot\,(\mathbf{r}, \mathbf{o})\right](u, v, \omega)$:

$\mathcal{S}(\mathbb{R}^6) \mapsto \mathcal{S}(\mathbb{R}^3)$ (which we call $\mathbb{A}_{\mathrm{DCT},(h,k,l)}(u,v,\omega;\mathbf{r},\mathbf{o})$ with a small abuse of notation) to the function $X(\mathbf{r},\mathbf{o})$, and the application of its adjoint, the integral back-projection operator $\mathbb{A}^{\dagger}_{\mathrm{DCT},(h,k,l)}[\cdot(u,v,\omega)](\mathbf{r},\mathbf{o}) : \mathcal{S}(\mathbb{R}^3) \mapsto \mathcal{S}(\mathbb{R}^6)$ (which we call $\mathbb{A}^{\dagger}_{\mathrm{DCT},(h,k,l)}(\mathbf{r},\mathbf{o};u,v,\omega)$, again with a small abuse of notation), to the function $B(u,v,\omega)$. The equivalents of operators $\mathbb{A}_{\mathrm{DCT},(h,k,l)}$ and $\mathbb{A}^{\dagger}_{\mathrm{DCT},(h,k,l)}$ for a generic transformation $\boldsymbol{D}$ that accepts ϕ values (different from 0) become $\mathbb{A}_{(h,k,l)}[\cdot(\mathbf{r},\mathbf{o})](u,v,\phi,\omega) : \mathbb{R}^3 \otimes \mathbb{O}^3 \mapsto \mathbb{R}^4$ and $\mathbb{A}^{\dagger}_{(h,k,l)}[\cdot(u,v,\phi,\omega)](\mathbf{r},\mathbf{o}) : \mathbb{R}^4 \mapsto \mathbb{R}^3 \otimes \mathbb{O}^3$ respectively. The point-wise intensity function from equation (C.5) becomes:

$$I(u,v,\phi,\omega,\mathbf{r},\mathbf{o}) = \delta\left(\mathbf{p}_{\mathrm{s}}(u,v,\phi,\omega,\mathbf{r}) - \hat{\mathbf{d}}_{\mathrm{s}}(\phi,\omega,\mathbf{o})\left(\mathbf{p}_{\mathrm{s}}(u,v,\phi,\omega,\mathbf{r})^T \cdot \hat{\mathbf{d}}_{\mathrm{s}}(\phi,\omega,\mathbf{o})\right)\right), \tag{C.8}$$

with: $\hat{\mathbf{d}}_{\mathrm{s}}(\phi,\omega,\mathbf{o}) = \hat{\mathbf{b}}_{\mathrm{s}}(\phi,\omega) + 2\left(\hat{\mathbf{b}}_{\mathrm{s}}(\phi,\omega)^T \cdot \mathbf{h}_{\mathrm{s}}(\mathbf{o})\right)\mathbf{h}_{\mathrm{s}}(\mathbf{o})$, and $\hat{\mathbf{b}}_{\mathrm{s}}(\phi,\omega) = \boldsymbol{D}^{-1}(\phi,\omega)\hat{\mathbf{b}}_{\mathrm{l}}$ where now we use the generic diffractometer transformation matrix $\boldsymbol{D}(\phi,\omega)$. The resulting generic versions of equations (C.6) and (C.7) are the equations (3) and (4) presented in section 2.5.

Operators $\mathbb{A}_{(h,k,l)}$ and $\mathbb{A}^{\dagger}_{(h,k,l)}$ suggest that adapting equations (3) and (4) to the TT projection geometry is trivial. The only caveat is that in one TT acquisition, we always look at the same lattice plane (h,k,l), and that we use the convention of grouping blobs in ϕ, while we separate them in ω. The TT versions of equations (3) and (4) can then be respectively derived as:

$$B'_{(h,k,l),\omega}(u,v,\phi) = \int_{\Omega_{\mathrm{R,O}}} X(\mathbf{r},\mathbf{o})\, I_{\omega}(u,v,\phi,\mathbf{r},\mathbf{o})\, C_{(h,k,l)}\, \mathrm{d}\mathbf{r}\mathrm{d}\mathbf{o}\,, \tag{C.9}$$

$$X'(\mathbf{r},\mathbf{o}) = \int_{\Omega_{\mathrm{D},\omega}} B_{(h,k,l),\omega}(u,v,\phi)\, I_{\omega}(u,v,\phi,\mathbf{r},\mathbf{o})\, C_{(h,k,l)}\, \mathrm{d}u\mathrm{d}v\,, \tag{C.10}$$

where the subscript ω indicates the fixed point in ω, and $\Omega_{\mathrm{D},\omega}$ is the support of the function $B_{(h,k,l),\omega}(u,v,\phi)$ for the said fixed ω.

Appendix D. More on alternative representations

This representation comes quite naturally from the joint use of Rodriguez space and the local mass fraction scalar function f. Another representation is based on unit quaternions for representing orientations, where the quaternions are multiplied by the mass fraction f. This other representation offers two

advantages over the previous representation: the space of the unit quaternions is *isochoric* (the density of the space is constant everywhere) [32], and for fractions $f = 0$ the representation is well behaved. In the first representation instead, the three orientation components are undefined for $f = 0$. Here, we prefer the first representation, because it leads to a simple definition of useful utility functions.

We split the vector function $\mathbf{X}(\mathbf{r})$ into the couple of functions $\mathbf{O}(\mathbf{r}) \in \mathcal{V}_3(\mathbb{R}^3) : \mathbb{R}^3 \mapsto \mathbb{O}^3 \subseteq \mathbb{R}^3$ and the previously defined $f(\mathbf{r}) \in \mathcal{S}(\mathbb{R}^3) : \mathbb{R}^3 \mapsto [0,1] \subset \mathbb{R}$. We obtain f using the "sum" operator $\mathbb{S}[\cdot(\mathbf{r},\mathbf{o})](\mathbf{r}) : \mathcal{S}(\mathbb{X}^6) \mapsto \mathcal{S}(\mathbb{R}^3)$, defined as:

$$f(\mathbf{r}) = \mathbb{S}[X(\mathbf{r},\mathbf{o})](\mathbf{r}) = \int_{\Omega_\mathrm{O}} X(\mathbf{r},\mathbf{o})\, \mathrm{d}\mathbf{o}\,. \tag{D.1}$$

We obtain $\mathbf{O}$ with the "mean" operator $\mathbb{M}[\cdot(\mathbf{r},\mathbf{o})](\mathbf{r}) : \mathcal{S}(\mathbb{X}^6) \mapsto \mathcal{V}_3(\mathbb{R}^3)$, defined as:

$$\mathbf{O}(\mathbf{r}) = \mathbb{M}[X(\mathbf{r},\mathbf{o})](\mathbf{r}) = \frac{\int_{\Omega_\mathrm{O}} \mathbf{o}\, X(\mathbf{r},\mathbf{o})\, \mathrm{d}\mathbf{o}}{\int_{\Omega_\mathrm{O}} X(\mathbf{r},\mathbf{o})\, \mathrm{d}\mathbf{o}}\,. \tag{D.2}$$

We can now rewrite the forward projection operator as the following:

$$B'_{(h,k,l)}(u,v,\phi,\omega) = \int_{\Omega_\mathrm{R}} f(\mathbf{r})\, I(u,v,\phi,\omega,\mathbf{r},\mathbf{O}(\mathbf{r}))\, C_{(h,k,l)}\, \mathrm{d}\mathbf{r}\,, \tag{D.3}$$

where now we only integrate over the position-space, whose support is Ω_R. In the same style of section 2.6, we can now write the matrix-vector representation of equation (D.3) as $\mathbf{b}_m = \boldsymbol{A}_m(\mathbf{x})\, \mathbf{x}$, where now the forward projection matrix depends on the solution vector $\mathbf{x}$.

Appendix E. Orientation space sensitivity

Given a one-dimensional line beam, each crystal lattice plane can be seen as a selective mirror that reflects only at certain incidence angles (Bragg angles). As a consequence, any rotation of the incidence beam around the plane normal is allowed. Moreover, if we only allow for deformation as rotations of the crystal (no elastic distortion of the unit-cell), then for a given plane normal in diffraction condition at $(\theta,\phi,\omega,\eta)$, we can only observe changes in ϕ, ω and η as the result of deformation (Bragg angles θ remain the same).

Each experimental setup offers different reconstruction sensitivities for certain directions along the coordinates of the orientation space, with respect to

changes in ϕ, ω and η on the blobs. This means that crystal rotations along certain directions in the sample coordinates can be more precisely determined using specific subsets of all the possible techniques. Here, we use simple arguments to give a basic understanding of this mechanism in the specific case of DCT and TT, while a more in depth and quantitative analysis is beyond the scope of this article.

In a DCT experiment, we can only observe changes in the data along ω and η. Sub-blob deviations in ω mainly correspond to rotations of the lattice around the sample z-axis ($\mathbf{z}_\mathrm{s}$), which corresponds to deviations in the z direction of the Rodrigues orientation space. Sub-blob deviations in η, instead, correspond mainly to rotations of the lattice around either the x-axis or the y-axis, depending on the ω at which they are observed. In fact, for a detector positioned perfectly perpendicular to the sample x-axis, as seen in section 2.2, the η angle is defined for rotations along such axis. This is valid for $\omega = z\pi$, with $z \in \mathbb{Z}$. When the sample is rotated by $\omega = (z + 1/2)\pi$, with $z \in \mathbb{Z}$, η is defined for rotations around the y-axis.

In a TT experiment, we can only observe changes along ϕ and η. For what concerns η changes, the same considerations of the DCT setup also apply to the TT geometry, for diffractometer sample tilts $\boldsymbol{R}_x$ and $\boldsymbol{R}_y$ equal or very close to 0. Also for what concerns ϕ, which is aligned with the sample y-axis, the same considerations hold, but with an additional rotation around ω by $\pi/2$. This means that ϕ changes relate to deformations along the y-axis for $\omega = z\pi$, and along the x-axis for $\omega = (z + 1/2)\pi$, with $z \in \mathbb{Z}$. In this case, different values of ω correspond to rotations around the selected plane normal, which does not provide additional information. For non negligible diffractometer sample tilts, the XY-plane in the sample coordinates is also tilted by the same $\boldsymbol{R}_x$ and $\boldsymbol{R}_y$ rotations. This means that η and ϕ changes correspond to deformations over the orientation space plane that is perpendicular to the selected plane normal. Due to the limited range of motion of the $\boldsymbol{R}_x$ and $\boldsymbol{R}_y$ tilt stages (on a typical instrument $\sim 10 - 20°$), this plane is always relatively close to the XY-plane in the sample coordinates.

In near-field experiments, however, η intermixes on the detector with the spatial coordinates. As a result, it is harder to resolve orientation changes from

η. Changes along ω for DCT experiments, and along ϕ for TT experiments, provide instead higher quality information, because they are not affected by the same problem. This means that DCT is more sensitive to deformations along the z-axis, while TT is more sensitive to deformations on a plane close to the XY-plane. For this reason, combining the two techniques can prove very beneficial to obtain higher quality and accuracy determination of the sub-grain crystal orientation.

Appendix F. Synthetic grain description

The synthetic grain used in section 3 is rendered in Fig. F.7(a), and it is composed of nine sub-grains. The sub-grains have an average grain bounding box diagonal of 50 μm, made exception for the central grain, whose diagonal is $\sim$ 82 μm. We present the plot of the kernel average misorientation (KAM) for the selected slice in Fig. F.7(b), and the intra-granular misorientation (IGM) in Fig. F.7(c). From Fig. F.7(b) we see that the strongest gradients of orientation can exceed 0.2 degrees over the length of one reconstruction voxel (0.75 μm), while in the selected slice the maximum misorientation from the central grain is around 0.3 degrees.

An isosurface of the synthetic grain orientation distribution function is presented in Fig. F.8, where the central sub-grain of Fig. F.7 has been highlighted by a red circle and a red arrow. Fig. F.8 shows the aforementioned division of the grain into a set of nine distinct sub-grains. Each of these sub-grains show small scale orientation variations (a few hundredths of a degree) due to the presence of orientation gradients

References

[1] J. Zhang, Y. Zhang, W. Ludwig, D. Rowenhorst, P. Voorhees, H. Poulsen, Three-dimensional grain growth in pure iron. Part I. statistics on the grain level, Acta Materialia 156 (2018). doi:10.1016/j.actamat.2018.06.021.

[2] Y. F. Shen, S. Maddali, D. Menasche, A. Bhattacharya, G. S. Rohrer, R. M. Suter, Importance of outliers: A three-dimensional study of coarsening in

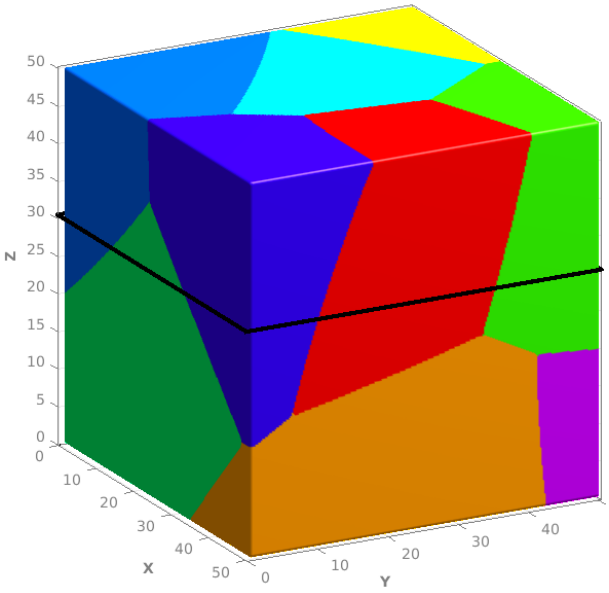

(a) Phantom 3D shape

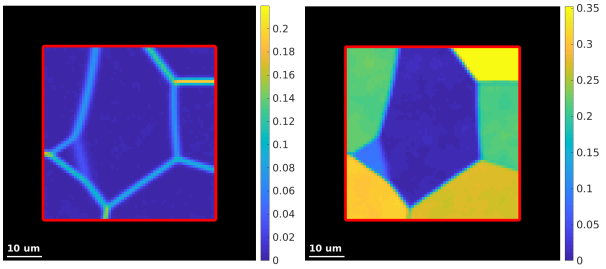

(b) Phantom KAM (c) Phantom IGM

Figure F.7: Synthetic grain summary representation: (a) 3D rendering of the synthetic grain, where the black horizontal slice indicates the slice used throughout section 3 for comparing the different methods; (b) the phantom kernel average misorientation in the said slice; (c) the intra-granular misorientation with respect to the central sub-grain in the said slice.

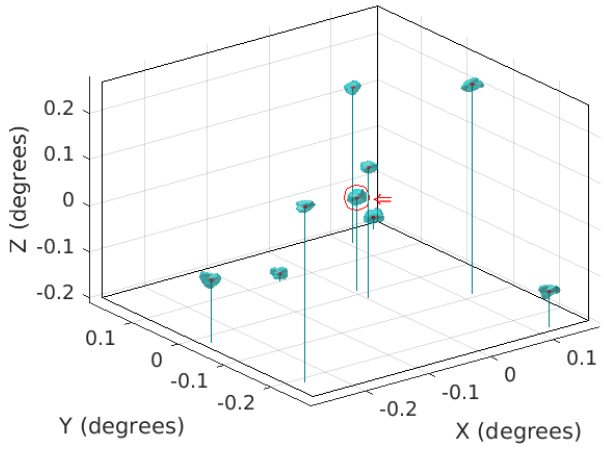

Figure F.8: The grain orientation distribution function. The red circle and arrow indicate the central and largest sub-grain. The axes are relative the orientation of the central grain.

α -phase iron, Physical Review Materials 3 (6) (jun 2019). doi:10.1103/PhysRevMaterials.3.063611.

[3] R. Pokharel, J. Lind, S. F. Li, P. Kenesei, R. A. Lebensohn, R. M. Suter, A. D. Rollett, In-situ observation of bulk 3D grain evolution during plastic deformation in polycrystalline Cu, International Journal of Plasticity 67 (2015) 217–234 (2015). doi:10.1016/j.ijplas.2014.10.013.

[4] P. A. Shade, W. D. Musinski, M. Obstalecki, D. C. Pagan, A. J. Beaudoin, J. V. Bernier, T. J. Turner, Exploring new links between crystal plasticity models and high-energy X-ray diffraction microscopy, Current Opinion in Solid State and Materials Science (2019). doi:10.1016/j.cossms.2019.07.002.

[5] A. King, G. Johnson, D. Engelberg, W. Ludwig, J. Marrow, Observations of Intergranular Stress Corrosion Cracking in a Grain-Mapped Polycrystal, Science 321 (5887) (2008) 382–385 (2008). doi:10.1126/science.1156211.

[6] M. Herbig, A. King, P. Reischig, H. Proudhon, E. M. Lauridsen, J. T. Marrow, J. Y. Buffiére, W. Ludwig, 3D growth of a short fatigue crack within a polycrystalline microstructure studied using combined diffraction

and phase-contrast X-ray tomography, Acta Materialia 59 (2011) 590–601 (2011).

[7] J. P. Hanson, A. Bagri, J. Lind, P. Kenesei, R. M. Suter, S. Gradečak, M. J. Demkowicz, Crystallographic character of grain boundaries resistant to hydrogen-assisted fracture in Ni-base alloy 725, Nature Communications 9 (1) (2018) 3386 (2018). doi:10.1038/s41467-018-05549-y.
URL https://doi.org/10.1038/s41467-018-05549-y

[8] P. Sedmák, J. Pilch, L. Heller, J. Kopeček, J. Wright, P. Sedlák, M. Frost, P. Šittner, Grain-resolved analysis of localized deformation in nickel-titanium wire under tensile load, Science 353 (6299) (2016) 559–562 (aug 2016). doi:10.1126/science.aad6700.

[9] A. N. Bucsek, L. Casalena, D. C. Pagan, P. P. Paul, Y. Chumlyakov, M. J. Mills, A. P. Stebner, Three-dimensional in situ characterization of phase transformation induced austenite grain refinement in nickel-titanium, Scripta Materialia 162 (2019) 361–366 (mar 2019). doi:10.1016/j.scriptamat.2018.11.043.

[10] P. Cloetens, W. Ludwig, J. Baruchel, D. Van Dyck, J. Van Landuyt, J. P. Guigay, M. Schlenker, Holotomography: Quantitative phase tomography with micrometer resolution using hard synchrotron radiation x rays, Applied Physics Letters 75 (19) (1999) 2912–2914 (nov 1999). doi:10.1063/1.125225.

[11] D. Paganin, S. C. Mayo, T. E. Gureyev, P. R. Miller, S. W. Wilkins, Simultaneous phase and amplitude extraction from a single defocused image of a homogeneous object, Journal of Microscopy 206 (1) (2002) 33–40 (apr 2002). doi:10.1046/j.1365-2818.2002.01010.x.

[12] W. Ludwig, P. Reischig, A. King, M. Herbig, E. M. Lauridsen, G. Johnson, T. J. Marrow, J. Y. Buffière, Three-dimensional grain mapping by x-ray diffraction contrast tomography and the use of Friedel pairs in diffraction data analysis., The Review of scientific instruments 80 (3) (2009) 033905 (mar 2009). doi:10.1063/1.3100200.

[13] W. Ludwig, E. M. Lauridsen, S. Schmidt, H. F. Poulsen, J. Baruchel, High-resolution three-dimensional mapping of individual grains in polycrystals by topotomography, Journal of Applied Crystallography 40 (5) (2007) 905–911 (oct 2007). doi:10.1107/S002188980703035X.

[14] A. Bonnin, J. P. Wright, R. Tucoulou, H. Palancher, Impurity precipitation in atomized particles evidenced by nano x-ray diffraction computed tomography, Applied Physics Letters 105 (8) (2014) 84103 (aug 2014). doi:10.1063/1.4894009.

[15] J. Oddershede, S. Schmidt, H. F. Poulsen, H. O. Sørensen, J. Wright, W. Reimers, Determining grain resolved stresses in polycrystalline materials using three-dimensional X-ray diffraction, Journal of Applied Crystallography 43 (3) (2010) 539–549 (jun 2010). doi:10.1107/S0021889810012963.
URL http://dx.doi.org/10.1107/S0021889810012963

[16] J. V. Bernier, N. R. Barton, U. Lienert, M. P. Miller, Far-field high-energy diffraction microscopy: a tool for intergranular orientation and strain analysis, The Journal of Strain Analysis for Engineering Design 46 (7) (2011) 527–547 (2011). doi:10.1177/0309324711405761.

[17] A. King, W. Ludwig, M. Herbig, J. Y. Buffiere, A. A. Khan, N. Stevens, T. J. Marrow, Three-dimensional in situ observations of short fatigue crack growth in magnesium, Acta Materialia 59 (17) (2011) 6761–6771 (2011). doi:DOI10.1016/j.actamat.2011.07.034.

[18] D. P. Naragani, P. A. Shade, P. Kenesei, H. Sharma, M. D. Sangid, X-ray characterization of the micromechanical response ahead of a propagating small fatigue crack in a Ni-based superalloy, Acta Materialia (2019). doi:10.1016/j.actamat.2019.08.005.

[19] R. M. Suter, D. Hennessy, C. Xiao, U. Lienert, Forward modeling method for microstructure reconstruction using x-ray diffraction microscopy: Single-crystal verification, Review of Scientific Instruments 77 (12) (2006) 123905 (2006). doi:10.1063/1.2400017.

[20] S. F. Li, R. M. Suter, Adaptive reconstruction method for three-dimensional orientation imaging, Journal of Applied Crystallography 46 (2) (2013) 512–524 (mar 2013). doi:10.1107/S0021889813005268.

[21] N. Gueninchault, H. Proudhon, W. Ludwig, Nanox: a miniature mechanical stress rig designed for near-field x-ray diffraction imaging techniques, Journal of Synchrotron Radiation 23 (6) (2016) 1474–1483 (nov 2016). doi:10.1107/S1600577516013850.

[22] H. Proudhon, N. Guéninchault, S. Forest, W. Ludwig, Incipient Bulk Polycrystal Plasticity Observed by Synchrotron In-Situ Topotomography, Materials 11 (10) (2018) 2018 (oct 2018). doi:10.3390/ma11102018.

[23] Y. Hayashi, D. Setoyama, Y. Hirose, T. Yoshida, H. Kimura, Intragranular three-dimensional stress tensor fields in plastically deformed polycrystals., Science (New York, N.Y.) 366 (6472) (2019) 1492–1496 (dec 2019). doi:10.1126/science.aax9167.
URL http://www.ncbi.nlm.nih.gov/pubmed/31857480

[24] H. Simons, A. King, W. Ludwig, C. Detlefs, W. Pantleon, S. Schmidt, F. Stöhr, I. Snigireva, A. Snigirev, H. F. Poulsen, Dark-field X-ray microscopy for multiscale structural characterization, Nature Communications 6 (1) (2015) 6098 (dec 2015). doi:10.1038/ncomms7098.

[25] H. F. Poulsen, P. K. Cook, H. Leemreize, A. F. Pedersen, C. Yildirim, M. Kutsal, A. C. Jakobsen, J. X. Trujillo, J. Ormstrup, C. Detlefs, Reciprocal space mapping and strain scanning using X-ray diffraction microscopy, Journal of Applied Crystallography 51 (5) (2018) 1428–1436 (2018). doi:10.1107/S1600576718011378.

[26] H. F. Poulsen, X. Fu, Generation of grain maps by an algebraic reconstruction technique, Journal of Applied Crystallography 36 (4) (2003) 1062–1068 (2003).

[27] N. Viganò, W. Ludwig, K. J. Batenburg, Reconstruction of local orientation in grains using a discrete representation of orientation space, Journal of Applied Crystallography 47 (6) (2014) 1826–1840 (oct 2014). doi:10.1107/S1600576714020147.

[28] N. Viganò, A. Tanguy, S. Hallais, A. Dimanov, M. Bornert, K. J. Batenburg, W. Ludwig, Three-dimensional full-field x-ray orientation microscopy, Scientific Reports 6 (feb 2016). doi:10.1038/srep20618.

[29] P. Reischig, A. King, L. Nervo, N. Viganó, Y. Guilhem, W. J. Palenstijn, K. J. Batenburg, M. Preuss, W. Ludwig, Advances in X-ray diffraction contrast tomography: flexibility in the setup geometry and application to multiphase materials, Journal of Applied Crystallography 46 (2) (2013) 297–311 (mar 2013). doi:10.1107/S0021889813002604.

[30] N. Viganò, L. Nervo, L. Valzania, G. Singh, M. Preuss, K. J. Batenburg, W. Ludwig, A feasibility study of full-field x-ray orientation microscopy at the onset of deformation twinning, Journal of Applied Crystallography 49 (2) (apr 2016). doi:10.1107/S1600576716002302.

[31] H. F. Poulsen, A six-dimensional approach to microtexture analysis, Philosophical magazine 83 (24) (2003) 2761–2778 (2003).

[32] F. C. Frank, Orientation mapping, Metallurgical Transactions A 19 (3) (1988) 403–408 (1988). doi:10.1007/BF02649253.

[33] A. Kumar, P. Dawson, Computational modeling of f.c.c. deformation textures over Rodrigues' space, Acta Materialia 48 (10) (2000) 2719–2736 (jun 2000). doi:10.1016/S1359-6454(00)00044-6.

[34] L. I. Rudin, S. Osher, E. Fatemi, Nonlinear total variation based noise removal algorithms, Physica D: Nonlinear Phenomena 60 (1-4) (1992) 259–268 (nov 1992). doi:10.1016/0167-2789(92)90242-F.

[35] M. Lang, H. Guo, J. E. Odegard, C. S. Burrus, R. O. Wells, Jr., Nonlinear processing of a shift invariant dwt for noise reduction, in: H. H. Szu (Ed.), Proc. SPIE Wavelet Applications II, Vol. 2491, 1995, pp. 640–651 (apr 1995). doi:10.1117/12.205427.

[36] S. J. Wright, Primal-dual interior-point methods, Vol. 117, SIAM, 1997 (1997). doi:10.1007/s10107-007-0168-7.

[37] A. Chambolle, T. Pock, A first-order primal-dual algorithm for convex problems with applications to imaging, Journal of Mathematical

Imaging and Vision 40 (1) (2010) 120–145 (dec 2010). doi:10.1007/s10851-010-0251-1.

[38] E. Y. Sidky, J. H. Jørgensen, X. Pan, Convex optimization problem prototyping for image reconstruction in computed tomography with the Chambolle-Pock algorithm, Physics in Medicine and Biology 57 (10) (2012) 3065–3091 (may 2012). doi:10.1088/0031-9155/57/10/3065.

[39] N. Viganò, W. Ludwig, Advances in 6d diffraction contrast tomography, Journal of Instrumentation 13 (04) (apr 2018). doi:10.1088/1748-0221/13/04/C04017.

[40] G. B. M. Vaughan, J. P. Wright, A. Bytchkov, M. Rossat, H. Gleyzolle, I. Snigireva, A. Snigirev, X-ray transfocators: Focusing devices based on compound refractive lenses, Journal of Synchrotron Radiation 18 (2) (2011) 125–133 (2011). doi:10.1107/S0909049510044365.

[41] H. Poulsen, W. Ludwig, E. Lauridsen, S. Schmidt, W. Pantleon, U. Olsen, J. Oddershede, P. Reischig, A. Lyckegaard, J. Wright, G. Vaughan, 4d characterization of metals by 3dxrd, in: Proceedings of the 31 Risø International Symposium on Materials Science, Vol. 31, Risø National Laboratory, 2010, pp. 101–119 (2010).

[42] H. Ibach, H. Lüth, Solid-State Physics, Advanced texts in physics, Springer Berlin Heidelberg, Berlin, Heidelberg, 2009 (2009). doi:10.1007/978-3-540-93804-0.

[43] H. F. Poulsen, Three-Dimensional X-Ray Diffraction Microscopy, Vol. 205 of Springer Tracts in Modern Physics, Springer Berlin Heidelberg, Berlin, Heidelberg, 2004 (2004). doi:10.1007/b97884.